

# A Consequent Pole Single Rotor Single Stator Vernier Design to Effectively Improve Torque Density of an Industrial PM Drive

Wenbo Liu, *Member, IEEE*, Jiyao Wang\*, *Member, IEEE*,  
and Thomas A. Lipo, *Life Fellow, IEEE*

**Abstract**—The vernier machine can utilize magnetic-gear effect, which conspicuously improves the torque production over other type of synchronous machines. However, a dual-rotor/dual-stator structure enabled high torque density vernier design is often unfavorable for industrial applications, due to manufacturing complexity and thermal management challenges. This paper successfully addresses this problem, by building magnetic-gear effect into a consequent pole enabled alternating flux barrier structure with single-rotor single-stator (SRSS). In this way, the proposed machine can achieve a superior torque density as a vernier machine does, while maintaining an equivalent manufacturing complexity as a conventional SRSS synchronous machine. This paper begins with elaborating generic analytical equations, that can transform into a vernier machine or a SRSS synchronous machine. More specifically, the magnetic-gear effect is manifested in the equations, via stator teeth originating flux modulation concept and resulting multi-harmonic field coupling effects. A SRSS vernier topology with consequent pole and V-shape magnet is then proposed. A considerable 52.6% improvement on the torque production with comparable efficiency are validated by experiments, where the comparison is made over that of a benchmark rare earth PM machine. Power factor would fall behind with increasing current load. Overall, this new design achieves an outstanding torque density, showing solid potential and feasibility for industry adoption.

**Index Terms**—consequent pole, V-shape magnet, rare earth magnet, high torque density low speed, vernier machine

## NOMENCLATURE

$\theta_s$	Spatial angle of the stator MMF.
$\theta_r$	Spatial angle of the rotor magnet MMF.
$\theta_{rm}$	Mechanical rotor rotation angle.
$k_h$	$h^{th}$ harmonic winding factor.
$N_s$	Total number of turns per phase.
$I_{pk}$	Stator peak current.
$C_p$	Number of parallel circuits.
$P_s, P_r$	Number of stator poles, and number of rotor poles.
$S_s$	Number of stator slots.
$\gamma$	Current phase shift angle.
$\gamma_0$	Stator slot pitch angle.
$\hat{p}_0, \hat{p}_h$	$dc$ and $h^{th}$ harmonic component of relative permeance
$l_{stk}$	Stack length.

## I. INTRODUCTION

THE vernier machine has been acknowledged for superior torque production capability due to its inherent magnetic-gear effect. The motor torque steps up as the rotor speed steps down from the normal synchronously rotating field. Since the debut a few decades ago [1], the torque density of the vernier machine has been improved by more than 10 times. Efforts have been devoted to applying various excitation methods and structure topologies to this type of machine. Three major advancements have been reported and verified in the experiment during this development era. The first advancement is to utilize the rotor field torque rather than the reluctance torque by replacing rotor reluctance teeth [1], [2] with surface mounted magnets [3], [4], [5], a superior torque density has been demonstrated compared to that of conventional PM machine. Then, a dual excitation/double stator structure [6] and double rotor structure [7] were proposed to further boost torque density where extra airgap areas were added for torque production. The third advancement has been known as the adoption of spoke type magnets in the double stator structure [8], which produces the highest torque density to date. The design features an opposing magnet arrangement on the rotor, in association with two stators offsetting by an angle, and hence the flux focusing effect is enabled and magnet leakage flux can be optimally reduced. Meanwhile, extensive attempts have been pursued to improve torque capability. A hybrid type excitation method was proposed in [9], [10] with the aim to combine the reluctance torque with field torque, where both windings and magnets are placed on the stator side. Another attempt is the axial flux design with a multi-stator/rotor structure [11]. Other attempts have been devoted to the improvement of electric loading, such as the usage of toroidal coils in the stator [12]. An alternative yet popular approach is to boost the magnetic loading in the airgap, where the interior flat magnets were replaced by different types of PM arrays. For example, spoke-type, V-type, and U-type were proposed to form individual rotor pole [13]–[16], such that more magnetic flux is generated at a price of high material cost. To achieve the same goal, Halbach PM array design with flux focusing effect was introduced to replace radially magnetized PM [17], at a relatively lower cost penalty. A step further on efficient magnetic flux generation is possible with consequent pole design, where rotor pole is formed by placing rectangular magnets on rotor surface [18], [19]. However, an inevitable drawback is the limited improvement on magnetic flux production due to the significantly reduced magnet usage. From technology adoption

(Corresponding author: Jiyao Wang, jyaowang@seu.edu.cn)

perspective, in contrast to the superior torque density that industry favors, there are some downsides in vernier machine, including its over-complicated structure for manufacturing and associated thermal management challenge, which both remain to be hurdles for industry adoption. Thus, it is appealing fill these gaps with a high torque density yet simple enough vernier design.

This paper proposes a vernier design that builds the magnetic-gear effect into a SRSS structure, where consequent pole enabled V-shape alternating flux barrier design is adopted on the rotor. The design efficiently uses the magnet pocket as the alternating flux barrier for maximizing winding fluxlinkage. To illustrate the concept, an analytical study of vernier machine and common synchronous machine is presented. A side-by-side comparison has been provided on the flux modulation effects and multi-harmonic fields coupling effects on both vernier machine and common synchronous machine. Given the benchmark design specifications, a V-shape magnet vernier machine is designed, followed by a genetic algorithm-based optimization for maximizing the torque density. Key results are compared among 2D, 3D predications and experiments. Good agreement can be obtained when 3D end effects are included in the FEA predication. Magnetic shear stress over magnet volume and over rotor volume are calculated and benchmarked with other cylindrical vernier machine designs from recent literatures. Results illustrate that the new design achieves an outstanding torque density in the class of SRSS vernier machine.

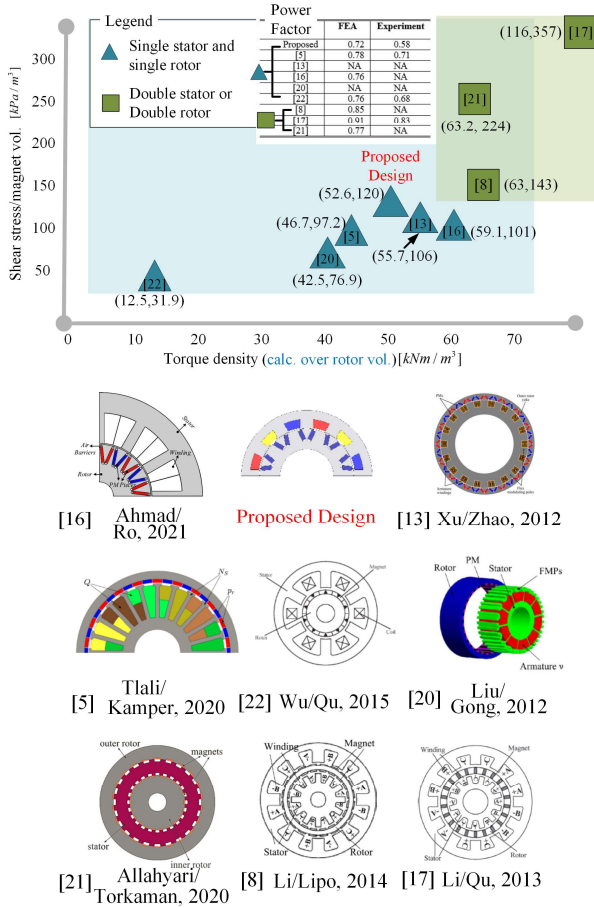


Fig. 1. Torque density map of cylindrical PM vernier machines in the existing literature.

## II. TORQUE DENSITY BENCHMARK COMPARISON

A torque density map summarizing the cylindrical PM Vernier machine performance of recent research [5], [13], [16], [17], [20]–[22] is given in Fig. 1. To assure a fair comparison, the motors all have similar armature current density level provided by fan-cooled or equivalent cooling methods, and the rotors all use the same type of rare earth magnet. The proposed consequent pole V-shape magnet vernier machine is also marked on the plot. The x-axis is the torque density over the rotor volume, indicating the torque capability of a given topology, and the y-axis is the magnetic shear stress over the magnet volume. To ensure a fair comparison across different machine size, the calculation is performed by scaling the machines to 150 mm OD. The scaled value become the indicator of the magnet cost of a certain design. The higher value, the more shear stress can be produced from the per unit volume magnet. The machine topology is differentiated by the triangle or square mark, corresponding to single stator/rotor design or double stator/rotor design. The light blue area and light green area denote the torque density for these two types of designs respectively. Coordinates under each mark/topology are the shear stress over the magnet volume and torque density over rotor volume. Therefore, a good design would always want to hit the upper right corner of the torque density map, which would consequently give out the best torque-capable design with lowest possible cost. Observations can be made as:

- Double stator or double rotor topologies generally produce more torque than single stator and rotor ones.
- The torque density per rotor volume indicates the machine performance, while the shear stress per magnet volume suggests the usage and cost of magnet for given output torque, for a given stack length, this value should be maximized for cost sensitive applications.
- The proposed V-shape magnet vernier machine has an outstanding torque density in single stator/rotor design, relaxed manufacturing complexity and moderate magnet cost.

## III. FLUX MODULATION EFFECTS IN VERNIER MACHINES AND COMMON SYNCHRONOUS MACHINES

Flux modulation effects and advantages of consequent pole have been explained and demonstrated in a vernier PM machine [15], [23], but in common SRSS synchronous machines, however, these stator teeth originated effects are historically treated as pure harmonic terms that contribute to zero average torque. It's a great opportunity if these effects can be appropriately modeled and applied to a SRSS machine to further increase its torque capability. Thus, to identify magnetic-gear effect in vernier machine and its inherent superior torque density, it is appealing to have a side-by-side comparison of flux modulation effects in vernier machines and in common synchronous machines. As shown in the following three subsections, the comparison will be based on key electromagnetic quantities using analytical equations.

### A. Rotor Flux Density in a Slotted Airgap

Stator teeth originated flux modulation effects are captured by modeling the rotor magnetic field variation, which is caused by a slotted/non-uniform airgap. As shown in Fig. 2, a rotor north pole is aligned with stator slot opening. Instead of

applying an effective/enlarged airgap to account for stator slot effects, a spatial distribution of flux density model should be adopted, such that the actual flux density distribution along the airgap circumference is captured as shown in Fig. 2(b), where flux density is more concentrated under the stator teeth than slots, acting as that the rotor flux is modulated.

If one ignores the leakage and fringing effects, then for a specific consequent pole design as shown in Fig. 3, the airgap flux density  $B_{rg}$  considering slot effects can be expressed as:

$$B_{rg} = B_{rg\_smooth} \hat{p} = \left[ \sum_{i=1}^{\infty} B_{mi} \sin \left( i \frac{P_r}{2} \theta_r \right) \right] \left[ \sum_{h=0}^{\infty} \hat{p}_h \cos(h S_s \theta_s) \right] \quad (1)$$

where flux density in a smooth airgap is  $B_{rg\_smooth} = \sum_{i=1}^{\infty} B_{mi} \sin \left( i \frac{P_r}{2} \theta_r \right)$ , and unitless relative permeance is  $\hat{p}_1 = f(\theta_s) = \sum_{h=0}^{\infty} \hat{p}_h \cos(h S_s \theta_s)$ , detailed derivation can be found in [23].

The airgap  $B$  field can be simplified by retaining the fundamental component ( $i = 1$ ) in  $B_{rg\_smooth}$  with the dc and fundamental ( $h = 0, 1$ ) components in  $\hat{p}$ , which have the largest magnitude. Setting  $\theta_s - \theta_r = \theta_{rm}$ , then (1) becomes

$$B_{rg} = B_{r1} \left[ \frac{1}{2} \hat{p}_1 \sin \left( \left( \frac{P_r}{2} - S_s \right) \theta_s - \frac{P_r}{2} \theta_{rm} \right) + \hat{p}_0 \sin \left( \frac{P_r}{2} (\theta_s - \theta_{rm}) \right) + \frac{1}{2} \hat{p}_1 \sin \left( \left( \frac{P_r}{2} + S_s \right) \theta_s - \frac{P_r}{2} \theta_{rm} \right) \right] \quad (2)$$

where  $B_{r1}$  is determined by the magnet material and usage.

For V-shape magnet, it would be mainly determined by the length and thickness according to [16]. The relative permeance can be explicitly expressed as functions of slot geometries namely  $\hat{p}_0(b_0/\tau_s, b_0/g)$  and  $\hat{p}_1(b_0/\tau_s, b_0/g)$ . This procedure has been thoroughly studied and the details can be found in [24], [25]. Thus, the analytical form of the resultant airgap  $B$  field is readily defined. For certain simple slot shapes, the relative permeance can be calculated with given parameters as shown in Fig. 4. The results suggest that:  $\hat{p}_0$  is 1 and  $\hat{p}_1$  is 0 with smooth/slotless stator when  $b_0/\tau_s$  or  $b_0/g$  is 0, corresponding to an absence of permeance variations. The difference between  $\hat{p}_0$  and  $\hat{p}_1$  begins to decrease as  $b_0/g$  and  $b_0/\tau_s$  increases, corresponding to a progressively larger permeance variation in the airgap.

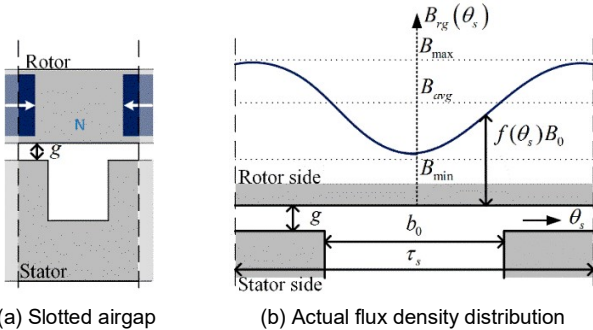


Fig. 2. Modeling of a slotted airgap for one magnetic pole considering flux modulation effects.

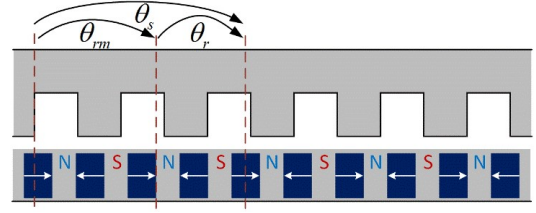


Fig. 3. Linearized model of a consequent pole PM machine.

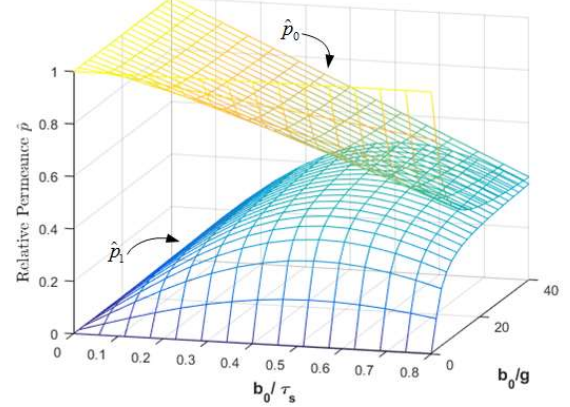


Fig. 4. Parametric study of the dc and fundamental components of relative permeance.

## B. No-Load Flux Linkage and Back-EMF Induction

A generic form of flux linkage can be derived by integrating an incremental flux linkage  $d\lambda$  over the stator circumference. Over one stator pole, assuming stator coils per phase are series connected:  $\lambda = \frac{1}{2} D_{is} l_{stk} \int_0^{2\pi/P_s} N(\theta_s) B_{rg}(\theta_s, \theta_{rm}) d\theta_s$ . The total flux linkage is then written as

$$\lambda = P_s \int_0^{2\pi/P_s} d\lambda = \frac{1}{2} D_{is} l_{stk} \int_0^{2\pi/P_s} N(\theta_s) B_{rg}(\theta_s, \theta_{rm}) d\theta_s = \frac{D_{is} l_{stk} N_s B_{r1} P_s}{\pi} \int_0^{2\pi/P_s} \left( \sum_{h=1,3,5}^{\infty} \frac{k_h}{h} \cos \left( h \frac{P_s}{2} \theta_s \right) \right) p_{sum} d\theta_s \quad (3)$$

Given that

$$p_{sum} = \frac{\hat{p}_1}{2} \sin \left( \left( \frac{P_r}{2} - S_s \right) \theta_s - \frac{P_r}{2} \theta_{rm} \right) + \hat{p}_0 \sin \left( \frac{P_r}{2} (\theta_s - \theta_{rm}) \right) + \frac{\hat{p}_1}{2} \sin \left( \left( \frac{P_r}{2} + S_s \right) \theta_s - \frac{P_r}{2} \theta_{rm} \right) \quad (4)$$

where the stator inner diameter  $D_{is}$  is used to approximate the airgap dimension for a inner-rotor machine configuration, and  $l_{stk}$  is stack length.

For a a balanced three-phase synchronous machine with  $P_s = P_r$ , and  $S_s = 3P_s q$ , the flux linkage can be explicitly expressed from (3) as

$$\lambda_{syn} = \frac{D_{is} l_{stk} N_s B_{r1}}{P_s} \frac{1}{2} \left[ \frac{k_{|1-6q|}}{|1-6q|} \hat{p}_1 + \frac{2k_1}{1} \hat{p}_0 + \frac{k_{1+6q}}{1+6q} \hat{p}_1 \right] \cos \left( \frac{P_r}{2} \theta_{rm} + \frac{\pi}{2} \right) \quad (5)$$

Similarly, for a a balanced three-phase vernier machine with  $P_r = (6q - 1)P_s$ , and  $S_s = 3P_s q$ , the flux linkage is

$$\lambda_{\text{vernier}} = \frac{D_{is} l_{stk} N_s B_{r1}}{P_s} \frac{1}{2} \left[ \frac{k_1}{1} \hat{p}_1 + \frac{2k_{6q-1}}{6q-1} \hat{p}_0 + \frac{k_{12q-1}}{12q-1} \hat{p}_1 \right] \cos\left(\frac{P_r}{2} \theta_{rm} + \frac{\pi}{2}\right) \quad (6)$$

By inspection, one can find that terms in the square bracket in (5) and (6) are different, suggesting two different sets of winding harmonics have been coupled with corresponding airgap  $B$  fields, this is because these two types of machine have different stator and rotor pole combinations. The back-EMF seen in the stator winding can then be calculated as the rate of change of no-load flux linkage over time,

$$e = \frac{d\lambda}{dt} = \frac{d\lambda}{d\theta_{rm}} \frac{d\theta_{rm}}{dt} = \omega_{rm} \frac{d\lambda}{d\theta_{rm}}$$

The back-emf for two types of machine are:

$$e_{\text{syn}} = \frac{D_{is} l_{stk} N_s B_{r1} \omega_{rm}}{2} \left[ \frac{k_1}{1-6q} \hat{p}_1 + \frac{2k_1}{1} \hat{p}_0 + \frac{k_{1+6q}}{1+6q} \hat{p}_1 \right] \cos\left(\frac{P_r}{2} \theta_{rm} + \frac{\pi}{2}\right) \quad (7)$$

$$e_{\text{vernier}} = \frac{P_r D_{is} l_{stk} N_s B_{r1} \omega_{rm}}{P_s} \left[ \frac{k_1}{1} \hat{p}_1 + \frac{2k_{6q-1}}{6q-1} \hat{p}_0 + \frac{k_{12q-1}}{12q-1} \hat{p}_1 \right] \cos\left(\frac{P_r}{2} \theta_{rm} + \frac{\pi}{2}\right) \quad (8)$$

### C. Torque Production

The torque produced in a rotating magnetic field can be calculated as

$$T_e = \frac{\partial}{\partial \theta_{rm}} \int_{V_{gap}} \frac{1}{2} B_{gap} H_{gap} dV_{gap} = \frac{D_{is} l_{stk}}{2} \int_0^{2\pi} \left( \frac{\partial}{\partial \theta_{rm}} B_{rg} \right) \mathcal{F}_{sg} d\theta_s \quad (9)$$

where the stator MMF is given in [26] as:

$$\mathcal{F}_{sg} = \frac{K_s D_{is}}{P_s} \sum_{h=1,5,7,\dots}^{\infty} \frac{k_{wh}}{h} \cos\left(h \frac{P_s}{2} \theta_s \pm (\omega_e t - \gamma)\right) \quad (10)$$

By incorporating (2) into (8), the torque equation becomes

$$T_e = \frac{D_{is}^2 l_{stk} K_s B_{r1} P_r}{4 P_s} \sum_{h=1,5,11,\dots}^{\infty} \frac{k_{wh}}{h} \int_0^{2\pi} \cos\left[h \frac{P_s}{2} \theta_s \pm (\omega_e t - \gamma)\right] \hat{p}_{sum} d\theta_s \quad (11)$$

So far, a generic form has been derived for an arbitrary synchronous machine, a more explicit expression can be easily developed for common synchronous machine and vernier machine separately for further comparison.

In a synchronous machine with  $P_s = P_r$ , and  $S_s = 3P_s q$ , equation (10) becomes

$$T_e = \frac{\pi D_{is}^2 l_{stk} K_s B_{r1} P_r}{4 P_s} \frac{1}{2} \left\{ \frac{k_{1+6q}}{1+6q} \hat{p}_1 \sin\left(\frac{P_r}{2} \theta_{rm} (\omega_e t - \gamma)\right) + \left( \frac{k_{1-6q}}{1-6q} \hat{p}_1 2k_1 \hat{p}_0 \right) \sin\left(\frac{P_r}{2} \theta_{rm} - (\omega_e t - \gamma)\right) \right\} \quad (12)$$

Here,  $P_r$  is intentionally left in the gear ratio term and the sine term for further comparison instead of replacing them with  $P_s$ . To produce average torque, rotor needs to be synchronized with electrical frequency as:  $\omega_e = \frac{P_r}{2} \frac{\theta_{rm}}{t} = \frac{P_r}{2} \omega_{rm}$ , such that the fundamental and  $|1-6q|$ <sup>th</sup> harmonics which are largest components are coupled, meanwhile,  $1+6q$ <sup>th</sup> harmonic becomes an oscillating term.

In a vernier machine where  $P_r = (6q-1)P_s$ , and  $S_s = 3P_s q$ , equation (11) can be simplified as:

$$T_e = \frac{\pi D_{is}^2 l_{stk} K_s B_{r1} P_r}{4 P_s} \frac{1}{2} \left[ \frac{k_1 \hat{p}_1 + 2 \frac{k_{6q-1}}{6q-1} \hat{p}_0 + \frac{k_{12q-1}}{12q-1} \hat{p}_1 \right] \times \sin\left(\frac{P_r}{2} \theta_{rm} + (\omega_e t - \gamma)\right) \quad (13)$$

Average torque can be produced if  $\omega_e = -\frac{P_r}{2} \frac{\theta_{rm}}{t} = -\frac{P_r}{2} \omega_{rm}$ . Suggesting that the current excitation need to rotate in the opposite direction along with rotor mechanical speed for all three harmonic components.

The above equations reveal the fundamentals of magnetic gear mechanisms, bridging the gap between vernier machines and common SRSS synchronous machines, making it possible to investigate magnetic gear effects in SRSS topologies. This opens great opportunities to extend the torque capability of a SRSS machine for industrial applications.

## IV. CONSEQUENT POLE VERNIER MACHINE DESIGN FOR AN INDUSTRIAL APPLICATION

The consequent pole V-shape vernier machine design is evolved from a previously reported consequent pole vernier machine, where spoke type magnets with alternating flux barrier was adopted [23]. The consequent pole V-shape design also enables the alternating flux barrier feature. Rare earth magnets are applied in this study for an industrial cooling fan application. Design details and application-oriented optimization are covered in the following subsections.

### A. Effective Magnet Utilization in Consequent Pole Enabled V-shape Alternating Flux Barrier Design

The alternating flux barrier structure has been found effective in improving magnet utilization in [23] with excessive amount of spoke type magnets. To reduce the magnet usage and costs while maintaining a good magnet flux utilization, a consequent pole V-shape magnet design is proposed. The magnets become flux source for rotor pole, and magnet pockets act as the alternating flux barriers that minimize local magnet leakage and maximize the winding fluxlinkage. Fig. 5(a) shows a regular V-shape design vernier machine with 4 stator-pole and 20 rotor-pole, all the rotor poles are formed by a pair of magnets, where white and green arrows denote different polarities. Fig. 5(b) shows a consequent pole V-shape design in the same design specs, the only difference is that Fig. 5(a) has double the number of magnets with half the length of that in the consequent pole V-shape. on the rotor side, two magnets with same polarity are set in a pair opposing with each other, such that a north (or south) pole is formed. Meanwhile, a pole with reverse polarity is also formed in between V-shape magnets. Thus, a consequent pole V-shape magnet design is obtained. This design also has the alternating flux barrier structure, as magnetic flux path has been provided between the pair-wise magnets. The benefits become apparent by comparing the no-load flux density distribution in Fig. 5(a) and (b), one can easily find that the consequent pole design has more fluxlinkage, which can be translated into a better magnet utilization under the same magnet usage. The airgap flux density and FFT analysis in Fig. (c) further qualitatively reveal that all three working harmonics in the consequent pole design are larger than its regular pole design counterparts. Given the noticeable difference, the consequent pole V-shape design is thus considered the main focus in the following analysis.



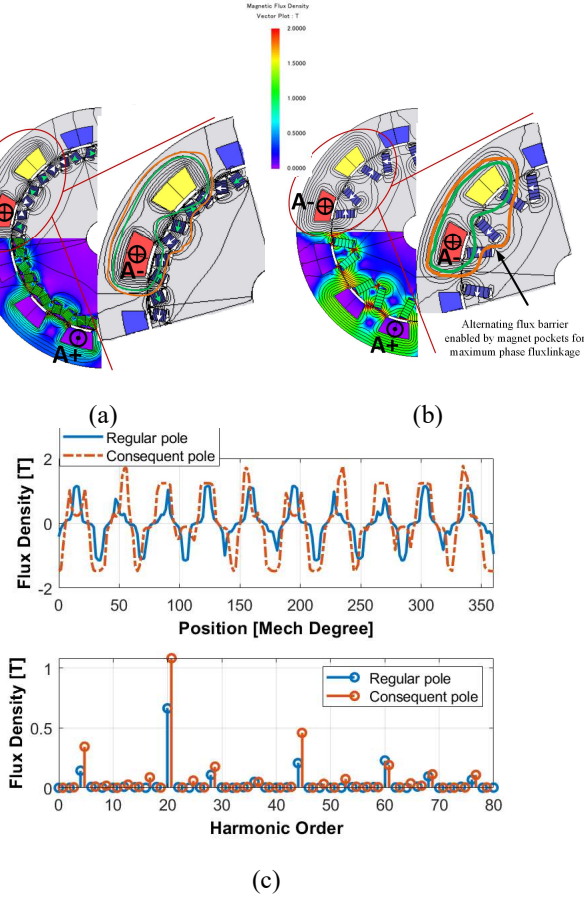


Fig. 5. Magnet induced flux density distribution comparison. (a) Regular V-shape vernier machine. (b) Consequent pole V-shape vernier machine with alternating flux barrier. (c) Center airgap flux density distribution and FFT analysis

### B. V-shape Consequent Pole Vernier Machine Design & 3D End Effects

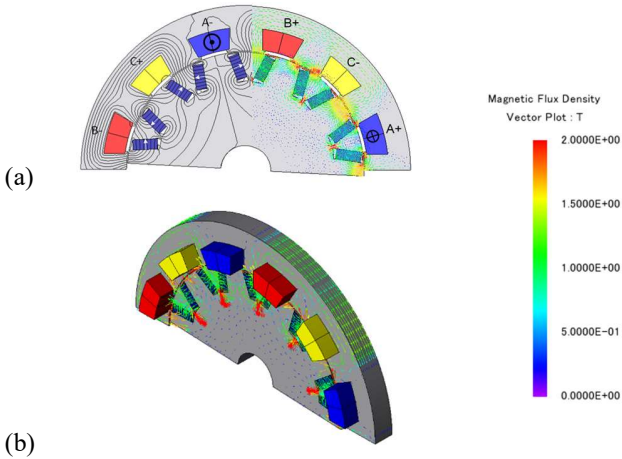


Fig. 6. No-load flux line distribution & vector in the slotted model. (a) 2D distribution. (b) 3D distribution.

Following the derivation from the previous section, a unity slot per pole per phase (SPP) value, 4 stator-pole and 20 rotor-pole with rare earth V-shape magnets design is shown in Fig. 6. The stator has 12 slots, and is configured as a 4-pole distributed winding design, phase sequence details are denoted, design choice details are provided in the following section. It

is clear to find that, even though the rotor is a 20-pole design, if seen from stator side, the major component of a 4-pole flux linkage path can be formed.

The 2D FEA assumes magnetic flux are confined within the 2D plane, as shown in Fig. 6. (a). This is true in most machine cross-section area. However, at the bottom bridge of magnet poles on the rotor, iron core is saturated, and the flux lines become red, indicating the flux density is around 2 T according to the magnetic flux density legend shown on the right side. As a result, the magnet flux tends to go through the rotor end in the axial direction in Fig. 6. (b) where some airspace is included in the flux path. Then, some flux leakage is formed in that direction, which is usually termed as 3D end effects in a cylindrical machine [26]. Thus, 2D analysis results would tend to overestimate a machine's electromagnetic (EM) performance. As a comparison, 3D results become more accurate on the FEA based estimation by including these 3D end effects. The next question to answer would be, to what extent the 3D end effects affect a machine EM performance. The following session aims to investigate this by benchmarking 2D, 3D and experiment results with each other for an industrial cooling fan application.

### C. Parameter Definition & Optimization for a Specific Application

To design a consequent pole V-shape magnet vernier machine for an industrial cooling fan application, it is necessary here to explain application design targets, constraints and identify machine geometry parameters along with associated FEA optimization results.

For this specific application, an air-cooled PM machine suitable for direct drive is required, as the machine needs to operate at 400 rpm and deliver 534 Nm torque in nominal condition. Due to the air cooling constrained thermal limit, the maximum allowable current density is set to 4.6 A/mm<sup>2</sup>. The magnet usage, stator diameter and stack length are also listed in Table I. All these specs are captured from a commercially available benchmark rare earth PM of a major motor manufacturer, where the benchmark PM is designed and manufactured for the same application. Meanwhile, the actual proposed prototype is sized to 1/6<sup>th</sup> of the full benchmark stack length for proof-of-concept demonstration. Thus, scaled benchmark specs are also provided in the table, they are used as the actual design constraints for prototype design.

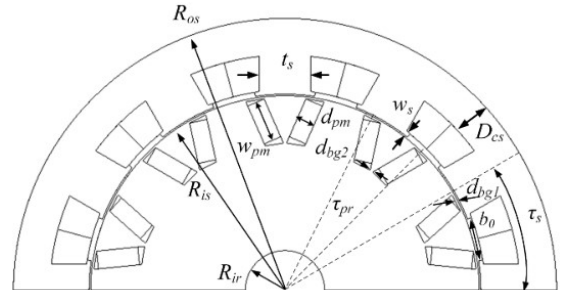


Fig. 7. Parametrization of the proposed machine geometry.

Critical design parameters need to be identified before further design exploration is pursued. First, the stator slot/pole number combination, number of turns, and slot filling factors

are chosen based on the target electric frequency, associated acceptable lamination hysteresis loss, inverter/drive specs and prototyping manufacturing capability. Then, for geometry design details, Fig. 7 illustrates parametric dimensions of the proposed consequent pole V-shape magnet design, where key parameters are parameterized to fully define the machine geometry.

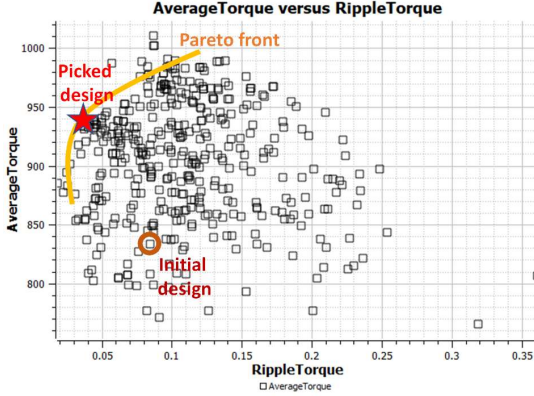


Fig. 8. Optimization for maximum average torque and minimum torque ripple at full stack length.

TABLE I  
SPECS FOR COMMERCIAL BENCHMARK MOTOR AND PROPOSED MOTOR

	Benchmark [27]	Proposed FEA
Machine type	IPM	VPM
Magnet type	NdFeB N40SH	
Mechanical speed $\omega_{rm}$ [rpm]	400	400
$J_s$ [A/mm <sup>2</sup> ]	4.6	4.6
Cu vol. (incl. end wind.) [L]	3.1	2.7
Stator OD [mm]	355.6	355.6
Total Magnet weight [kg]	11.3	11.2
Stator/rotor poles	4/4	4/20
SPP	4	1
Excitation frequency [Hz]	13.33	66.67
Stator slots number	48	12
Active stack length [mm]	311.15	311.15
Airgap [mm]	1	1
Output Torque [Nm]	534	940
Active Volume [m <sup>3</sup> ]	0.031	0.031
Active Volume Torque Density [Nm/L]	17.3	30.4
Power Factor	0.8	0.72
Torque Ripple [%]	4%	4%

A design of experiment (DOE) table needs to be generated to initiate the optimization. The optimization process was pursued using the software built-in multi-objective genetic algorithm, two key objective functions are set in the optimization to meet design targets listed in Table. I:

$$\text{Obj1: } \max(T_e) \quad (14)$$

$$\text{Obj2: } \min\left(\frac{\max(T_e) - \min(T_e)}{\text{avg}(T_e)}\right) \quad (15)$$

Subject to  $D_{cs}, D_{ls}, D_{cr}, t_s, \tau_s, w_{pm}, d_{bg1}, d_{bg2}, w_b, d_b$  in geometry boundaries.

The optimization results for machine geometry in Table II is tabulated for the proposed topology, where maximizing the average torque and minimizing the ripple torque are set as the primary optimization target. Fig. 8 shows the optimization analysis results. To achieve optimization target with given

constraints, the red star is selected from the identified Pareto front. It should be noted that the selected design is obtained with a full stack length analysis, a fine-tuning process is also conducted for manufacturing process. As a result, the final design electromagnetic performance would be a little different as shown in later plots.

TABLE II  
INITIAL AND OPTIMIZED KEY DIMENSIONS

	Optimized	Initial Design
Stator OR/IR [mm]	177.8/128.3	177.8/130.8
Rotor OR/IR [mm]	127.3/17.7	129.8/17.7
$D_{cs}$ [mm]	23.9	22.5
$\tau_s$ [°]	30	30
$\tau_{pr}$ [°]	18	18
$t_s$ [mm]	34	28
$d_{pm}/w_{pm}$ [mm]	11.7/27	10/24
$d_{bg1}/d_{bg2}$ [mm]	1.35/1.15	0.7/1
$w_s/b_\theta$ [mm]	2.65/30	0.8/30

## V. EXPERIMENT SETUP AND RESULTS VALIDATION

This section would first introduce the assembly of V-shape magnet prototype machine along with the test dynamometer setup, then present measured data and FEA predictions. ;

### A. Manufactured Prototype Machine and Experiment Set-up

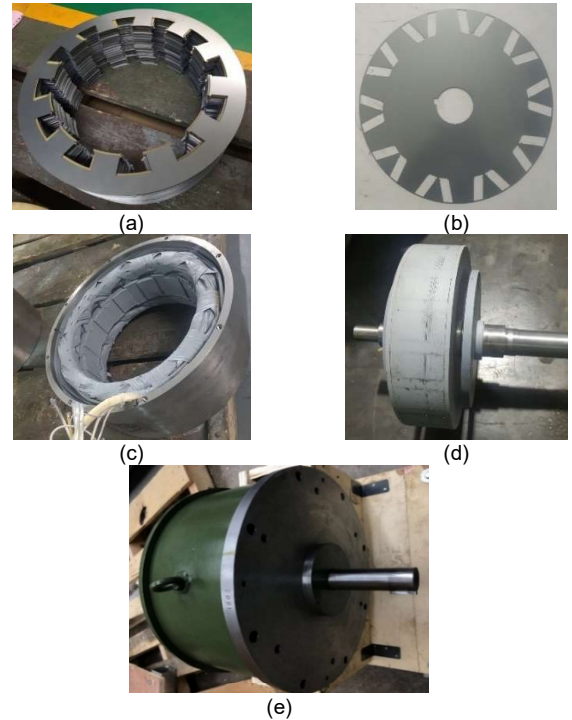


Fig. 9. Assembly of V-shape prototype machine (a) Stator Laminations (b) Rotor Laminations (c) Stator stack in the housing (d) Rotor stack with inserted magnets (e) Full assembly

Fig. 9. shows the assembly of the prototype machine. The stator and rotor laminations are laser cut using 50WW600 cold-rolled non-oriented electrical steel with a lamination thickness of 0.5mm. The lamination designs are provided in Fig. 9. (a) and (b), with stator lamination on the left and rotor on the right. A keyway structure is added to the rotor shaft hole, such that the rotor laminations can slide onto the shaft and obtain a firm installation.

The stator assembly is shown in Fig. 9. (c), where the stator laminations are installed to the housing, and windings are inserted with the same polyester material applied. 0.4 slot fill factor is assumed for manual winding process. One can also find that the end winding part takes a large portion of the full stack length. This end winding would lead to extra copper losses, which can be mitigated in a full scaled machine. The complete rotor assembly is provided in Fig. 9. (d), the grey color comes from the polyester material used to prevent oxidation and degradation of assembled parts. After the magnets are inserted into rotor laminations, two non-magnetic end plates are installed at rotor ends to prevent the axial movement of these magnets. Fig.9. (e) is a picture of the full assembly, the housing of which is made of structure steel covered by anti-corrosion coating. Stator part is press fit into the housing, and the rotor part is installed to the shaft through keyway, then the whole rotor assembly is held by bearings installed to two end plates. Since the machine is designed to be running continuously under air cooled current density condition, no cooling system was added to the prototype assembly.

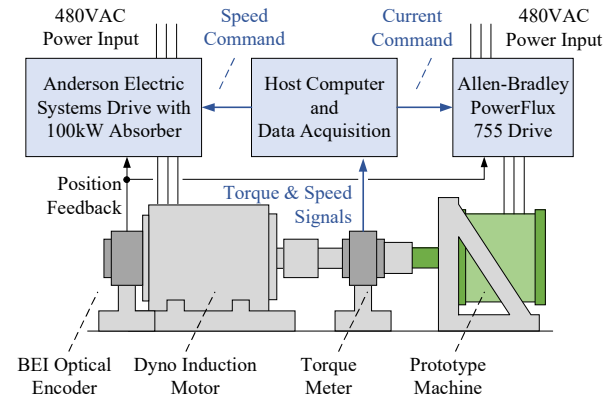


Fig. 10. Dynamometer setup for prototype motor test

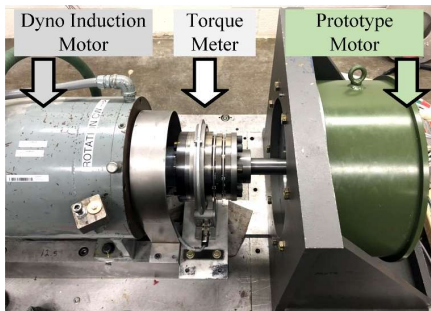


Fig. 11. Dynamometer test bench for the prototype vernier PM machines

A schematic configuration of the dynamometer setup in the lab is shown in Fig. 10. The manufactured prototype machine is connected to the dyno induction motor via a torque meter,

where the dyno motor is driven by an Anderson Electric Controls Absorber drive, and the prototype machine is driven by Allen-Bradley PowerFlex 755 AC Drive. The position sensor is mechanically mounted on the dyno motor side but electrically connected to both drives, so the prototype and dyno motor can share the same encoder feedback signal. During the test, the prototype motor is running at torque regulation mode with current command, and the dyno side is regulating the speed. Since the prototype machine would only be driven in the motoring region, the power would be drawn from the grid through the prototype machine, and delivered to the dyno machine, and the generated power would be then fed back to the grid through the absorber drive. Fig. 11 shows the dynamometer testbench setup, where the dyno motor is mounted onto the left motor mounting stand with foot mount, and the prototype motor is mounted to the motor mounting stand on the right with a face mount. The dyno induction motor is rated 97kW, with 128.6 Nm (150% peak torque for 3 seconds) continuous torque and 7200 rpm base speed. It should be noted that the prototype machine winding turns and stack length are scaled to accommodate the inverter and test dyno setup. For the cooling system, an oil cooled jacket is installed around stator. The HBM T10F/FS torque flange is used for the torque measurement, it is rated for 500 Nm nominal torque with max. speed of 12000 rpm.

## B. Discussion and Benchmarking of FEA & Test Results

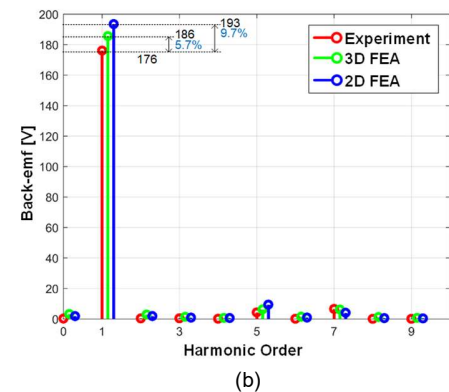
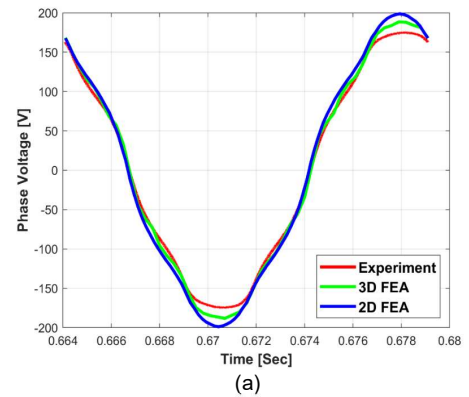


Fig. 12. Line to line back-EMF comparison at 400 rpm rotor speed (a) Waveform (b) FFT analysis.

Fig. 12 shows the back-EMF waveform in line to line values, the measured experiment data are compared to FEA results both in 2D and 3D analysis. The waveforms are compared in Fig. 12 (a), the profile of which suggests a good



agreement between experiment results and FEA calculations. However, a certain discrepancy is observed, according to the FFT analysis of this back-EMF in Fig. 12 (b) in a detailed comparison. A 9.7% difference in fundamental component is shown between experiment and 2D FEA analysis, the difference is reduced to 5.7% by comparing with 3D FEA analysis. This is mainly caused by the machine end effects, which are usually more noticeable for pancake shape radial flux machine with short stack length. Besides, the difference between experiment and 3D FEA results could come from the difference between the magnet property in prototype and the corresponding datasheet used in FEA simulation, where actual magnets magnetization state and operating temperature are hard to accurately capture.

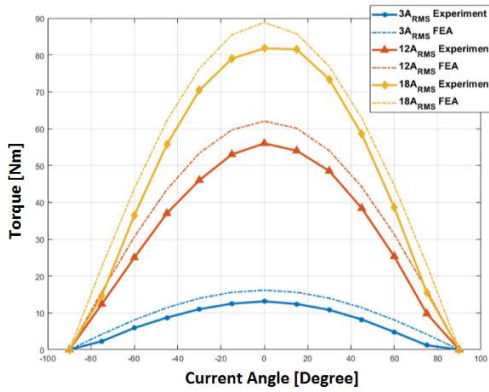


Fig. 13. Torque vs. current angle at different current level.

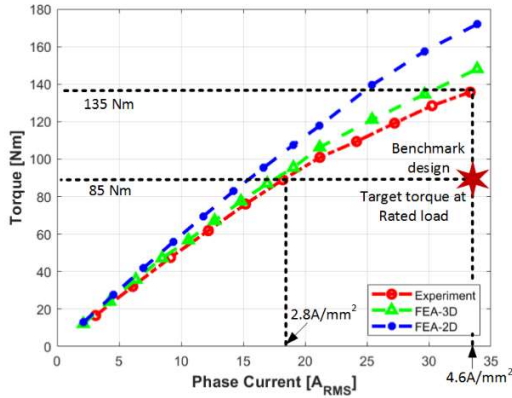


Fig. 14. Torque capability vs. current at the MTPA operating point.

The vernier machine is known for non-salient behavior, which also applies to the proposed design, even though it has an apparent salient pole rotor. The non-salient feature is enabled because the rotor saliency is averaged out from 5 to 1 rotor to stator pole design, such that the  $d$ - and  $q$ - axis both have the flux paths that goes through the machine laminations without penetrating the inserted magnet. Thus, the prototype machine is more like a surface PM machine with a small airgap. In a non-salient machine, the maximum torque value can be reached at current angle 0 where the current vector is aligned to  $q$ - axis in the synchronous frame. To verify this non-salient magnetic behavior, a torque vs. current angle analysis is carried out at different current level as shown in Fig. 13. Both the measured values and FEA predicated results reach the

maximum at 0 current angle, a sinusoidal waveform is obtained consistently across 3 different current levels, from the light load condition to rated load condition. Thus, the non-magnetic behavior was confirmed for the prototype machine. It also should be noted that, the FEA calculation is carried out in 2D analysis, which tends to overestimate the torque production, detailed explanation would be given in the following torque capability analysis.

A torque capability vs. current at MTPA operating point analysis was carried out in Fig. 14. Experimental results are compared with FEA predictions. The 3D FEA predication is generally more accurate than that of 2D FEA, it is again because the end effects are modeled in the 3D analysis. One can conclude that the end effects become more critical in the FEA modeling accuracy as the current load increases, when the saturation in the iron bridge or tooth tips is expected.

TABLE III

PERFORMANCE COMPARISON COMMERCIAL BENCHMARK MOTOR AND PROPOSED MOTOR

	IPM		Proposed @ Rated Torque Load		Proposed @ Rated Current Density	
Stack Length [mm]	311.15	50	311.15	50	311.15	50
$J_s$ [A/mm <sup>2</sup> ]	4.6		2.8		4.6	
Output Torque [Nm]	534	86	534	86	840	135
Torque Density* [Nm/L]	17.3	17.3	17.3	17.3	27.2	27.2
Mechanical Speed [rpm]	400		400		400	
Excitation Frequency [Hz]	13.33		66.67		66.67	
Output Power [kW]	22.3	3.6	22.3	3.6	35.2	5.6
Winding Losses [kW]	NA		0.7	0.3	2.3	1.1
Core & PM Losses [kW]	NA		1.1	0.18	1.3	0.2
Efficiency [ $\eta$ %]	92%	NA	93%	88%	91%	81%
Power Factor [p.u.]	0.8	0.8	0.7	0.7	0.58	0.58

\*The value is calculated based on the machine active volume

Table III summarize the performance comparison between the commercial benchmark motor and the proposed motor. The experimental result suggest that the target torque can be produced by the prototype machine at 2.8A/mm<sup>2</sup>, which is much less than the 4.6A/mm<sup>2</sup> used in the benchmark motor to produce the same amount of torque, the corresponding efficiency is 88% due to the scaled stack length, the power factor is 0.7. If the prototype machine is to be operated at 4.6A/mm<sup>2</sup>, 135 Nm torque can be produced with 0.58 power factor, which corresponds to 27.2 Nm/L over total machine volume. The efficiency is impaired for 50mm stack prototype, this is mainly caused by the relatively large end-winding resistance. The efficiency gets improved in the full stack length with less end-winding effect. The torque capability/torque density is increased by 52.6% under the same current density and similar magnet usage. Prototype results are promising and provide extra design freedom for target application, for example, prototype machine can be operated at a much lower current density for better efficiency, or a smaller and more cost effective design can be obtained by leveraging improved torque capability. Overall, the results validate the high torque



capability/torque density of the prototype machine predicated by the FEA calculations.

## VI. CONCLUSION

A consequent pole V-shape vernier machine with high torque density has been presented for an industrial PM drive application. Analytical form of back-emf induction and torque production equations are derived, for both vernier machine and common synchronous machine. Comparison has been focused on the flux modulation effects and multi-harmonic fields coupling effects. FEA optimization and predication are further conduct using benchmark design specs. Key results are compared between 2D, 3D predications and verified by experiments, good agreement can be obtained if 3D end effects are included in the FEA predication. Non-salient electromagnetic behavior is also identified and studied. The torque production has been improved by 52.6% compared with that of a benchmark rare earth magnet assisted PM under the same stator current density. Torque density over magnet volume and rotor volume are calculated and benchmarked against other cylindrical vernier machine designs in recent literatures. Showing that this design not only proves to be the most torque-dense in the single rotor vernier machine, but also achieves comparable torque capability of a double rotor design. Overall, the simple structure and good torque capability make this proposed consequent pole V-shape vernier machine an attractive and practical candidate for low-speed applications. Going beyond the motor component level study, it would be beneficial to look at the scalability analysis among all possible alternatives, and electric drive system level design for optimum performance in suitable user-case, such as industrial cooling fans, wind turbines, and marine propulsion.

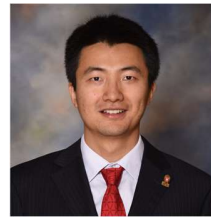
## ACKNOWLEDGMENT

The authors express their gratitude to the companies of the Wisconsin Electric Machines and Power Electronics Consortium (WEMPEC), and Robert Draper Technology Innovation Fund provided by Wisconsin Alumni Research Foundation (WARF) for assistance and support during this research.

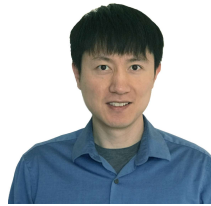
## REFERENCES

- [1] G. Kronacher, "Design, performance and application of the Vernier resolver," *The Bell System Technical Journal*, vol. 36, no. 6, pp. 1487–1500, 1957.
- [2] C. H. Lee, "Vernier motor and its design," *IEEE Trans. Power Appar. Syst.*, vol. 82, no. 66, pp. 343–349, 1963.
- [3] A. Ishizaki, T. Tanaka, K. Takahashi, and S. Nishikata, "Theory and Optimum Design of PM Vernier Motor." *Electrical Machines and Drives Seventh International Conf.*, Durham, UK, 1995.
- [4] Y. Oner, Z. Q. Zhu, L. J. Wu, X. Ge, H. Zhan, and J. T. Chen, "Analytical On-Load Subdomain Field Model of Permanent-Magnet Vernier Machines," *IEEE Trans. Ind. Electron.*, vol. 63, no. 7, pp. 4105–4117, Jul. 2016, doi: 10.1109/TIE.2016.2532285.
- [5] P. M. Tlali, R.-J. Wang, S. Gerber, C. D. Botha, and M. J. Kamper, "Design and Performance Comparison of Vernier and Conventional PM Synchronous Wind Generators," *IEEE Trans. Ind. Appl.*, vol. 56, no. 3, pp. 2570–2579, May 2020, doi: 10.1109/TIA.2020.2979111.
- [6] A. Toba and T. A. Lipo, "Novel dual-excitation permanent magnet vernier machine," in *Industry Applications Conference, 1999. Thirty-Fourth IAS Annual Meeting. Conference Record of the 1999 IEEE*, 1999, vol. 4, pp. 2539–2544. Accessed: Jul. 27, 2016. [Online]. Available: [http://ieeexplore.ieee.org/xpls/abs\\_all.jsp?arnumber=799197](http://ieeexplore.ieee.org/xpls/abs_all.jsp?arnumber=799197)
- [7] S. Niu, S. L. Ho, W. N. Fu, and L. L. Wang, "Quantitative Comparison of Novel Vernier Permanent Magnet Machines," *IEEE Trans. Magn.*, vol. 46, no. 6, pp. 2032–2035, Jun. 2010, doi: 10.1109/TMAG.2010.2042429.
- [8] D. Li, R. Qu, and T. A. Lipo, "High-Power-Factor Vernier Permanent-Magnet Machines," *IEEE Trans. Ind. Appl.*, vol. 50, no. 6, pp. 3664–3674, Nov. 2014, doi: 10.1109/TIA.2014.2315443.
- [9] E. Spooner and L. Haydock, "Vernier hybrid machines," *IEE Proc. - Electr. Power Appl.*, vol. 150, no. 6, p. 655, 2003, doi: 10.1049/ip-epa:20030909.
- [10] S. Jia, R. Qu, J. Li, D. Li, and H. Fang, "Hybrid excited vernier PM machines with novel DC-biased sinusoidal armature current," Sep. 2016, pp. 1–8. doi: 10.1109/ECCE.2016.7855174.
- [11] F. Zhao, T. A. Lipo, and B.-I. Kwon, "A Novel Dual-Stator Axial-Flux Spoke-Type Permanent Magnet Vernier Machine for Direct-Drive Applications," *IEEE Trans. Magn.*, vol. 50, no. 11, pp. 1–4, Nov. 2014, doi: 10.1109/TMAG.2014.2329861.
- [12] T. Zou, D. Li, R. Qu, J. Li, and D. Jiang, "Analysis of a Dual-Rotor, Toroidal-Winding, Axial-Flux Vernier Permanent Magnet Machine," *IEEE Trans. Ind. Appl.*, pp. 1–1, 2017, doi: 10.1109/TIA.2017.2657493.
- [13] G. Xu, L. Jian, W. Gong, and W. Zhao, "Quantitative Comparison of Flux-modulated Interior Permanent Magnet Machines with Distributed Windings and Concentrated Windings," *Prog. Electromagn. Res.*, vol. 129, pp. 109–123, 2012, doi: 10.2528/PIER12040901.
- [14] R. Hosoya, H. Shimada, and S. Shimomura, "Design of a ferrite magnet vernier machine for an in-wheel machine," in *2011 IEEE Energy Conversion Congress and Exposition*, Phoenix, AZ, USA, Sep. 2011, pp. 2790–2797. doi: 10.1109/ECCE.2011.6064144.
- [15] W. Liu and T. A. Lipo, "A family of vernier permanent magnet machines utilizing an alternating rotor leakage flux blocking design," in *Energy Conversion Congress and Exposition (ECCE), 2017 IEEE*, 2017, pp. 2461–2468.
- [16] H. Ahmad and J.-S. Ro, "Analysis and Design Optimization of V-Shaped Permanent Magnet Vernier Motor for Torque Density Improvement," *IEEE Access*, vol. 9, pp. 13542–13552, 2021, doi: 10.1109/ACCESS.2021.3052258.

- [17] D. Li, R. Qu, and Z. Zhu, "Comparison of Halbach and Dual-Side Vernier Permanent Magnet Machines," *IEEE Trans. Magn.*, vol. 50, no. 2, pp. 801–804, Feb. 2014, doi: 10.1109/TMAG.2013.2280760.
- [18] S.-U. Chung, J.-W. Kim, B.-C. Woo, D.-K. Hong, J.-Y. Lee, and D.-H. Koo, "A Novel Design of Modular Three-Phase Permanent Magnet Vernier Machine With Consequent Pole Rotor," *IEEE Trans. Magn.*, vol. 47, no. 10, pp. 4215–4218, Oct. 2011, doi: 10.1109/TMAG.2011.2157324.
- [19] H. Wang *et al.*, "A Novel Consequent-Pole Hybrid Excited Vernier Machine," *IEEE Trans. Magn.*, vol. 53, no. 11, pp. 1–4, Nov. 2017, doi: 10.1109/TMAG.2017.2695494.
- [20] G. Liu, J. Yang, W. Zhao, J. Ji, Q. Chen, and W. Gong, "Design and Analysis of a New Fault-Tolerant Permanent-Magnet Vernier Machine for Electric Vehicles," *IEEE Trans. Magn.*, vol. 48, no. 11, pp. 4176–4179, Nov. 2012, doi: 10.1109/TMAG.2012.2204042.
- [21] A. Allahyari and H. Torkaman, "A Novel High-Performance Consequent Pole Dual Rotor Permanent Magnet Vernier Machine," *IEEE Trans. Energy Convers.*, vol. 35, no. 3, pp. 1238–1246, Sep. 2020, doi: 10.1109/TEC.2020.2980146.
- [22] L. Wu, R. Qu, D. Li, and Y. Gao, "Influence of Pole Ratio and Winding Pole Numbers on Performance and Optimal Design Parameters of Surface Permanent-Magnet Vernier Machines," *IEEE Trans. Ind. Appl.*, vol. 51, no. 5, pp. 3707–3715, Sep. 2015, doi: 10.1109/TIA.2015.2426148.
- [23] W. Liu and T. A. Lipo, "Analysis of Consequent Pole Spoke Type Vernier Permanent Magnet Machine With Alternating Flux Barrier Design," *IEEE Trans. Ind. Appl.*, vol. 54, no. 6, pp. 5918–5929, Nov. 2018, doi: 10.1109/TIA.2018.2856579.
- [24] B. Heller and V. Hamata, *Harmonic Field Effects in Induction Machines*. Amsterdam, The Netherlands: Elsevier, 1977.
- [25] Z. Q. Zhu, D. Howe, E. Bolte, and B. Ackermann, "Instantaneous magnetic field distribution in brushless permanent magnet DC motors. I. Open-circuit field," *IEEE Trans. Magn.*, vol. 29, no. 1, pp. 124–135, 1993.
- [26] T. A. Lipo, *Introduction to AC machine design*, First Edition. Hoboken, New Jersey: John Wiley & Sons, Inc., 2017.
- [27] Z. S. Du and T. A. Lipo, "Torque Performance Comparison Between a Ferrite Magnet Vernier Motor and an Industrial Interior Permanent Magnet Machine," in *IEEE Transactions on Industry Applications*, vol. 53, no. 3, pp. 2088–2097, May-June 2017, doi: 10.1109/TIA.2017.2673812.



**Wenbo Liu** received B.S. from Xi'an Jiaotong University, Xi'an, Shaanxi, China, and Ph.D from University of Wisconsin-Madison, WI, USA, in 2012 and 2019 respectively, both in Electrical Engineering. From 2019, He is with Research and Innovation Center at Ford Motor Company, Dearborn, USA, where he has been working on the electric motor and control system of Ford Hybrids, Electric Vehicles and Plug-Ins. His research focus is high performance electric drive system including electric machine design and control.



**Jiayao Wang** received B.S. degree from Tsinghua University, Beijing, China, and Ph.D from University of Wisconsin-Madison, WI, USA, in 2010 and 2015 respectively, in electrical engineering. From 2016 to 2020 he was with Ford Motor Company, Dearborn, USA, where he was part of the Product Development team for the electric motor control and drive system of Ford and Lincoln brand production level electric vehicles including F150 Hybrid, Aviator Hybrid, and Mustang Mach-E. In 2021 he joined the Department of Electrical Engineering, Southeast University, Nanjing, China. His primary research interests are the designs and controls for the integration of electric machine drive system.



**Thomas A. Lipo** is an IEEE Life Fellow, IET(London) Fellow Retired, Member of the National Academy of Engineering (USA), the Royal Academy of Engineers (UK) and the National Academy of Inventors (USA). He earned his BEE with Honors from Marquette University in Milwaukee, WI, in 1962 as well as his MSEE in 1964. He then completed his PhD work at the University of Wisconsin-Madison in 1968. Before returning to UW-Madison as an Electrical Engineering Professor and the co-founder/director of the research group WEMPEC in 1981, Dr. Lipo worked for Allis-Chalmers Manufacturing Company, Milwaukee, WI, and General Electric in Schenectady, NY. He was also Professor in the Department of Electrical Engineering at Purdue University in West Lafayette, IN, 1980-81. Dr. Lipo has been a visiting fellow at the University of Manchester Institute of Science and Technology, Cambridge University and Sheffield University, in England; and the University of Sydney, and Monash University, Australia. He was a Fulbright Fellow at University of Trondheim, Norway in 2008. Dr. Lipo has received many awards from IEEE Societies including the IEEE Medal for Power Engineering. He retired from UW-Madison in 2009 and is presently hold the position of Research Professor at Florida State University, Tallahassee, Florida.